ACS APPLIED MATERIALS & INTERFACES

www.acsami.org

Research Article

Experimental and Computational Investigation of Layer-Dependent Thermal Conductivities and Interfacial Thermal Conductance of One- to Three-Layer WSe_2

Elham Easy, Yuan Gao, Yingtao Wang, Dingkai Yan, Seyed M. Goushehgir, Eui-Hyeok Yang, Baoxing Xu,* and Xian Zhang*

Cite This: https://dx.doi.org/10.1021/acsami.0c21045

Read Online

ACCESS | Metrics & More | Article Recommendations | Supporting Information

ABSTRACT: Two-dimensional materials such as graphene and transition metal dichalcogenides (TMDCs) have received extensive research interest and investigations in the past decade. In this research, we used a refined opto-thermal Raman technique to explore the thermal transport properties of one popular TMDC material WSe_2, in the single-layer (1L), bilayer (2L), and trilayer (3L) forms. This measurement technique is direct without additional processing to the material, and the absorption coefficient of WSe_2 is discovered during the measurement process to further increase this technique's precision. By comparing the sample's Raman spectroscopy spectra through two different laser spot sizes, we are able to obtain two parameters—lateral thermal conductivities of 1L−3L WSe_2 and the interfacial thermal conductance between 1L−3L WSe_2 and the substrate. We also implemented full-atom nonequilibrium molecular dynamics simulations (NEMD) to computationally investigate the thermal conductivities of 1L−3L WSe_2 to provide comprehensive evidence and confirm the experimental results. The trend of the layer-dependent lateral thermal conductivities and interfacial thermal conductance of 1L−3L WSe_2 is discovered. The room-temperature thermal conductivities for 1L−3L WSe_2 are 37 ± 12, 24 ± 12, and 20 ± 6 W/(m·K), respectively. The suspended 1L WSe_2 possesses a thermal conductivity of 49 ± 14 W/(m·K). Crucially, the interfacial thermal conductance values between 1L−3L WSe_2 and the substrate are found to be 2.95 ± 0.46, 3.45 ± 0.50, and 3.46 ± 0.45 MW/(m^2·K), respectively, with a flattened trend starting the 2L, a finding that provides the key information for thermal management and thermoelectric designs.

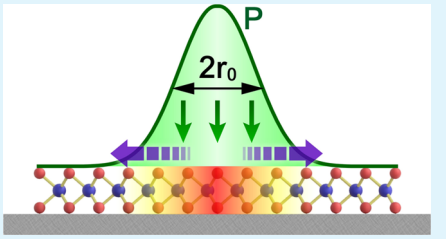

KEYWORDS: *tungsten diselenide, Raman spectroscopy, thermal conductivity, interfacial thermal conductance, layer-dependent trend*

INTRODUCTION

Since graphene's first isolation by mechanical exfoliation in 2004,[1−3] two-dimensional (2D) materials have received extensive attention due to their unique atomically thin structures and novel physical properties.[4−23] In particular, transition metal dichalcogenide (TMDC) materials have shown intriguing thermal, thermoelectric, electrical and optical properties, such as enhanced figure of merit, prominent band structure, and semiconducting behavior, which distinguish them from graphene.[8−10,24−33] This makes TMDC materials an ideal candidate for the next-generation thermal, thermoelectric, electrical, and optical applications. Although the thermal properties of common TMDC materials, i.e., 2D MoS_2 and $MoSe_2$, have been studied extensively both experimentally and theoretically,[30,32,34−43] the investigation of the emerging thermoelectric material WSe_2 has received much less attention. On the other hand, 2D WSe_2 has emerged as a promising thermoelectric candidate due to a high Seebeck coefficient of 680 μV/K,[69] compared to 280 μV/K for Bi_2Te_3, a commercial thermoelectric material. There is an increasing layer-dependent trend of the Seebeck coefficient and a decreasing trend of the thermal conductivity of WSe_2, leading to a high figure of merit with the layer number. Thus, discovering the thermal conductivities of 2D WSe_2 and the layer-dependent trend is of fundamental importance and also lays immediate guides to the development of flexible thin-film thermoelectric devices, thereby revolutionizing both the fundamental thermal transport of materials and application technologies in thermoelectric devices.

While the electrical and optical properties of 2D WSe_2 have been extensively studied,[44−51] there is no experimental research reported on thermal transport properties in 2D WSe_2. The computational studies of WSe_2's thermal transport properties have the results in the large range of 0.2−22 W/(m·K),[52−57] which motivates experimental investigation and verification. Meanwhile, a low thermal conductivity in the range of 1.2−1.6 W/(m·K) was found for disordered layered

Received: November 25, 2020
Accepted: March 5, 2021

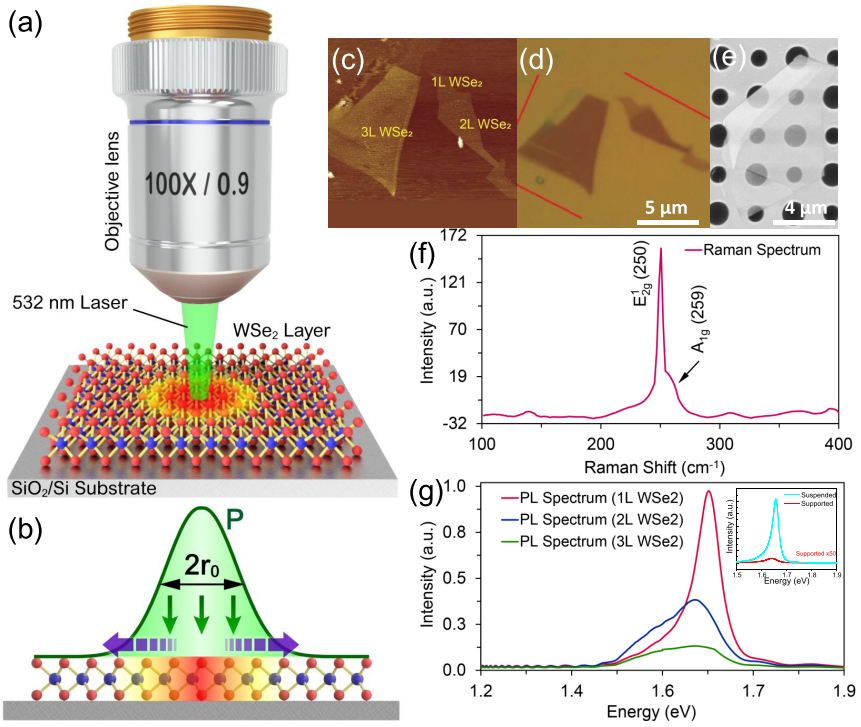

Figure 1. (a) Schematic of the experimental setup for the WSe_2 sample by the opto-thermal Raman technique. (b) Schematic of the Raman laser and thermal transport profiles. (c) Atomic force microscopy image of 1L−3L WSe_2. (d) Optical microscopy image of 1L−3L WSe_2. (e) Scanning electron microscopy image of the suspended 1L WSe_2 on the holes. (f) Raman spectrum of 2D WSe_2 with two characteristic peaks (E_{2g}^1 and A_{1g}). (g) Photoluminescence spectra of 1L−3L WSe_2. The inset shows the photoluminescence spectra of the supported and suspended areas specifically.

WSe_2 in the bulk form by both the electrical heating method and the time-domain thermoreflectance (TDTR) method.[58,59] In a recent thermal measurement based on TDTR, a thermal conductivity value of 42 W/(m·K) was discovered for the ordered crystalline layered WSe_2 in the bulk form.[60] Therefore, it is needed to conduct a comprehensive experimental thermal investigation of WSe_2 in the 2D atomic-layered forms (single layer, bilayer, and trilayer) to discover the intrinsic in-plane thermal conductivities and the interfacial thermal conductance of 2D WSe_2 and investigate their layer dependence.

In this letter, we demonstrate the measurement of the thermal conductivities of single-layer (1L), bilayer (2L), and trilayer (3L) WSe_2 and their interfacial thermal conductance to the substrate, via a well-developed opto-thermal Raman technique for discovering the thermal properties of TMDCs in the 2D form. We also carefully measured the absorption coefficients of 1L−3L WSe_2 during the measurement process. The systematic experimental results provide a layer number-dependent analysis. The opto-thermal Raman technique has been the most suitable method for measuring the thermal conductivity of 2D materials with thicknesses down to subnanometer.[20,30,37] Compared to the TDTR method, which is famous for its capability of measuring the thermal conductivities of 2D materials in the bulk form,[61] and the electrical heating method,[59] which is renowned for its reliability in high-resolution temperature calibration for 2D bulk materials, the opto-thermal Raman technique is fit for measuring the intrinsic thermal conductivities of 2D materials with thicknesses down to subnanometer. In the opto-thermal Raman technique, a laser is focused on the sample and the position of the Raman peaks is utilized as the benchmark. As the laser power increased, the sample gets heated, which enables red-shift Raman mode due to thermal softening. Thermal conductivity is then calculated from the thermal modeling based on the measured Raman position shift rate. In addition, the thermal modeling requires the input of several key parameters: Raman peak position shift with temperature, optical absorbance, and the interfacial thermal conductance between WSe_2 and the substrate. The retrieved room-temperature thermal conductivities and interfacial thermal conductance of 1L−3L WSe_2 are the first reported experimental results. In summary, the opto-thermal Raman technique-based measurement is conducted at a steady state and is independent of time, during which a Raman laser is focused on the sample surface and used as both a heat source and a temperature prober. As the heat source, laser power is absorbed uniformly throughout the thickness, making it an ideal method in measuring the thermal conductivities of samples with the smallest existing thickness (subnanometer). In addition, the non-contact measurement method has the minimum fabrication requirement and thus maintains the sample's pristine physical properties.

RESULTS AND DISCUSSION

Figure 1a presents the schematic of WSe_2 on the SiO_2/Si substrate with the opto-thermal Raman measurement technique by a 532 nm wavelength laser. Figure 1b shows the laser profile and thermal transport schematic in WSe_2. Figure 1c shows the atomic force microscopy (AFM) topography of 1L, 2L, and 3L WSe_2 flakes obtained by mechanical exfoliation, with the optical microscopy image shown in Figure 1d as a reference. The mechanical exfoliation method has been key in providing high-quality 2D materials, ensuring the pristine physical properties of the sample. The thicknesses of 1L−3L WSe_2 samples are confirmed by AFM. The detailed AFM information is recorded in the Supporting

https://dx.doi.org/10.1021/acsami.0c21045
ACS Appl. Mater. Interfaces XXXX, XXX, XXX−XXX

Table 1. First-Order Temperature Coefficients, Absorbance, and Power Shift Rates of 1L−3L WSe_2

				absorbed power shift rate ($cm^{-1}/\mu W$)	
		temperature coefficient (cm^{-1}/K)	absorbance (%)	0.18 μm spot	0.26 μm spot
1L WSe_2	supported	−0.0187 ± 0.0022	5.8 ± 1.1	−0.0225 ± 0.0024	−0.0124 ± 0.0150
1L WSe_2	suspended	−0.0226 ± 0.0025	5.7 ± 1.1	−0.1385 ± 0.0129	
2L WSe_2	supported	−0.0147 ± 0.0019	11.1 ± 2.1	−0.0142 ± 0.0028	−0.0080 ± 0.0123
3L WSe_2	supported	−0.0132 ± 0.0004	16.3 ± 2.8	−0.0125 ± 0.0004	−0.0071 ± 0.0002

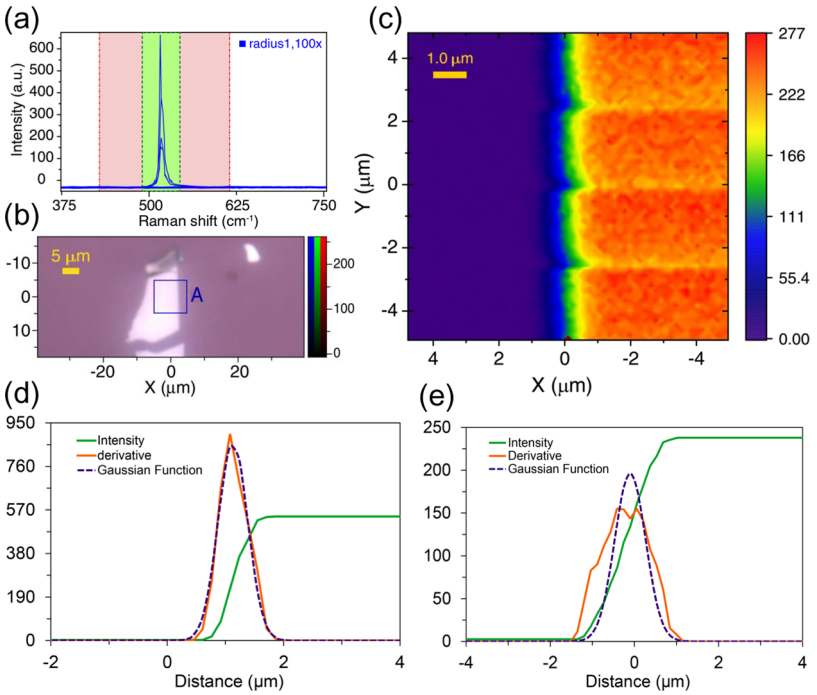

Figure 2. (a) Raman spectra mapping monitoring the Si peak. (b) Optical microscopy image and (c) 10 μm × 10 μm micro-Raman mapping across a sharp flake edge. The Raman intensity (green) and the extracted profile of the laser beam (orange) as a function of the beam position for the laser spot from 100× objective (d) and 40× objective (e).

Information. Figure 1e presents the scanning electron microscopy (SEM) image of the suspended 1L WSe_2 sample on 1 and 1.5 μm diameter holes. Figure 1f demonstrates the Raman spectrum of WSe_2 by the 532 nm wavelength laser, with E_{2g}^1 and A_{1g} peaks. The E_{2g}^1 peak is used as the characterization peak for the thermal transport measurement due to its clear and accurate signal. Figure 1g shows the photoluminescence spectra of 1L−3L by the 532 nm wavelength laser, which reconfirms the 1L WSe_2 because it has a direct band gap, which is presented as a single peak photoluminescence (PL) curve. 1L WSe_2 has only one peak at about 1.65 eV, while 2L and 3L WSe_2 have a PL peak at around 1.63 eV. The peak intensity of 1L WSe_2 at 1.65 eV is at least 2.5 times that of 2L WSe_2 at 1.63 eV, in accordance with the previous report.[33] PL curves also show that the suspended WSe_2 has a PL peak intensity that is more than 500 times that of the supported WSe_2, which reconfirms the suspended condition.

During the measurement process, a Raman laser with a wavelength of 532 nm is focused on WSe_2 through the microscope objective, and the thermal flow provided by the laser is propagating isotropically in all radial directions from the laser position. Here, we are considering measured temperature, laser spot size, absorption coefficient of the sample, and laser power. The 40× and 100× microscope objectives were used to generate two laser spot sizes, providing enough experimental data to obtain the two key parameters—in-plane thermal conductivity and interfacial thermal conductance. To determine the heat source, which is the laser power absorbed for the thermal transport analysis, another group of 1L−3L WSe_2 from the same crystal source was prepared on the transparent quartz substrates, and their optical absorption spectra were measured to determine the frequency-dependent complex dielectric function. The dielectric functions of the target sample material and that of the substrate material were used to calculate the absorption coefficient at a wavelength of 532 nm based on the standard transfer matrix method. The absorption coefficient α of WSe_2 can be determined by optical transmittance T_e taken from the measurements and calculated based on the following equation[62]

$$T_e = \frac{(1-R)^2 \exp(-\alpha d)}{1 - R^2 \exp(-2\alpha d)} \quad (1)$$

where d is the target sample thickness and R is a function of the refractive index n: $R = (n - 1/n + 1)^2$, with n reconfirmed from ref 29. The obtained α is 894734 cm^{-1} at a wavelength of 532 nm. The obtained optical absorbance values of 1L−3L WSe_2 are 5.7 ± 1.1, 10.9 ± 2.1, and 16.0 ± 2.8% at a wavelength of 532 nm. These values can be used for the suspended WSe_2 sample. For the supported WSe_2, the optical

https://dx.doi.org/10.1021/acsami.0c21045
ACS Appl. Mater. Interfaces XXXX, XXX, XXX−XXX

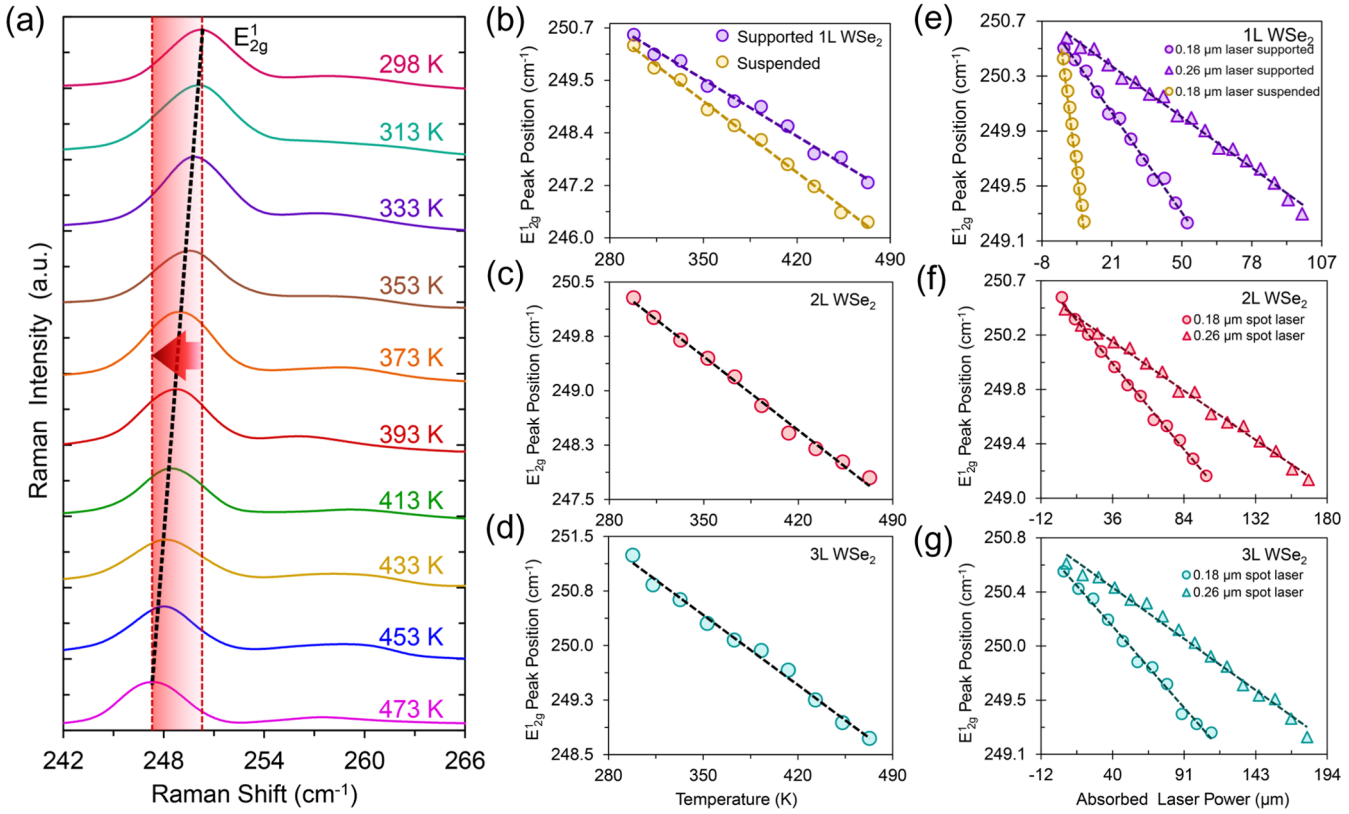

Figure 3. (a) Raman spectra of 1L WSe_2 recorded at temperatures from 298 to 473 K. The temperature-dependent E_{2g}^1 Raman peak shift measured on the 1L WSe_2 both supported and suspended (b), 2L WSe_2 (c), and 3L WSe_2 (d). Power-dependent E_{2g}^1 Raman peak shift measured using different laser spot sizes, on the 1L WSe_2 both supported and suspended (e), 2L WSe_2 (f), and 3L WSe_2 (g).

interference effect from the substrate (285 nm SiO_2 on Si) was taken into account to calculate the absorbance, with results summarized in Table 1. Because of the low quantum yield of as-exfoliated 1L WSe_2,[70−73] which is in the range of 0.03−3%, the absorbed energy emitting as photons is ignored.

The laser beam spot (r_0) is characterized by moving the laser across a sharp edge based on which the Raman laser profile is following a Gaussian distribution. Figure 2a shows the Raman spectroscopy mapping across a sharp edge to monitor the Si peak. The mapping frequency range is 500−550 cm^{-1} to monitor the Si peak. Figure 2b,c shows the optical microscopy image and 10 μm × 10 μm micro-Raman mapping. The Si peak intensity was studied as a function of the moving position (dI/dx) with Gaussian distribution ($K{\cdot}\exp(-(x-a)^2/r_0^2)$) fitting (Figure 2d,e). Through characterization and fitting, the laser spot size passing through the 100× objective is determined as 0.18 ± 0.02 μm and that passing through the 40× objective is determined as 0.26 ± 0.02 μm. r_0 can also be estimated from the numerical aperture estimation: $r_0 = \lambda/(\pi{\cdot}NA)$, where NA is the numerical aperture value of the objectives, and NA values for 100× and 40× objectives are 0.9 and 0.75, respectively. r_0 values were calculated as 0.19 and 0.23 μm, respectively. These estimated values are close to the experiment results.

The Raman laser was used both as a heat source and for temperature characterization. We first calibrated the Raman E_{2g}^1 peak position's shift rate at temperatures ranging from 298 to 473 K. A laser with a wavelength λ of 532 nm was used. Figure 3a presents the Raman spectra of 1L WSe_2 with temperature dependence. Figure 3b shows the temperature-dependent Raman E_{2g}^1 peak position shift of 1L WSe_2 in both supported and suspended forms. The peak position's linear red shift is caused by the bond softening that is thermally driven, which is consistent with the previous studies on graphene, MoS_2, and $MoSe_2$.[30] The suspended sample has a larger thermally driven bond softening due to the larger in-plane lattice expansion in the suspended condition. Figure 3c,d presents the temperature dependence of the E_{2g}^1 peak shift for 2L and 3L WSe_2, showing the same red shift. The linear temperature-dependent shift rate of the E_{2g}^1 peak is defined as the first-order temperature coefficient (Table 1). It is found that the first-order temperature coefficient decreases with the layer number, and this decreasing trend is consistent with the previous work on MoS_2 and $MoSe_2$,[30] due to the fact that with the increasing layer number of 2D WSe_2, the temperature-dependent in-plane lattice expansion coefficient decreases.

In the second part of the thermal measurements, laser power-dependent Raman spectra were taken to extract the linear relation between the sample temperature and the absorbed laser power. The E_{2g}^1 Raman peak shift was fit as a function of the absorbed laser power for the 1L−3L WSe_2 samples, and two laser spots with sizes of 0.18 and 0.26 μm were used. Figure 3e−g presents the laser power-dependent Raman peak shift rates of the supported 1L−3L WSe_2 and suspended 1L WSe_2. The obtained absorbance, temperature coefficients, and absorbed laser power shift rates of 1L−3L WSe_2 are summarized in Table 1.

The schematic of the laser heating process at a steady state in WSe_2 is shown in Figure 1a,b. The temperature distribution in the cylindrical coordinate $T(r)$ is related to the absorbed laser power, in-plane thermal conductivity, and the interfacial thermal conductance between the sample and the substrate.[30]

https://dx.doi.org/10.1021/acsami.0c21045
ACS Appl. Mater. Interfaces XXXX, XXX, XXX−XXX

The heat convection from WSe_2 to air is less than 0.01% of the total heat in the thermal transport process and is thus ignored (see the Supporting Information). The absorbed laser power P is determined by the multiplication of the actual laser power and the sample's optical absorbance (Table 1). Based on the Gaussian profile of the laser and its spot size r_0, the volumetric laser heating power density $q'''(r)$ is presented as

$$q'''(r) = P \cdot \frac{1}{t} \cdot \frac{1}{\pi r_0^2} \exp\left(-\frac{r^2}{r_0^2}\right) \tag{2}$$

where t is the thickness of WSe_2. Considering the interfacial thermal conductance between WSe_2 and the substrate, $T(r)$ is expressed as

$$\frac{1}{r}\frac{d}{dr}\left(r\frac{dT(r)}{dr}\right) - \frac{g}{k_s t}(T(r) - T_a) + \frac{q'''(r)}{k_s} = 0 \tag{3}$$

where T_a is the substrate temperature, κ_s is the in-plane thermal conductivity of WSe_2 in the supported condition, and g is the interfacial thermal conductance between WSe_2 and the substrate. COMSOL Multiphysics simulations have shown that the substrate temperature T_a also increases with laser heating, and the ratio between the temperature increase of WSe_2 and SiO_2 is used for obtaining the interfacial thermal conductance g (see the Supporting Information). The boundary conditions $(dT)/(dr)|_{r=0} = 0$ for laser's Gaussian profile and $T(r \to \infty) = 0$ for room temperature at the edge of the sample are applied. For the suspended sample, $g = 0$.

The average temperature of WSe_2 within the laser spot is characterized by the E_{2g}^1 peak position using the Raman peak shift rate given in Table 1. The average temperature is a weighted result by considering the Gaussian profile of the laser spot

$$T_m = \frac{\int_0^\infty T(r) \exp\left(-\frac{r^2}{r_0^2}\right) r dr}{\int_0^\infty \exp\left(-\frac{r^2}{r_0^2}\right) r dr} \tag{4}$$

The fitted Raman peak shift rates from the experimental results in Figure 3 are summarized in Table 1. The measured thermal resistance of WSe_2 can be calculated as $R_m = T_m/P$. To calculate the WSe_2 thermal conductivity κ_s and interfacial thermal conductance to the substrate g, we followed the method by Cai et al.[37] Equations 2−4 provide an expression of R_m as a function of κ_s and g. Specifically, the ratio of two measured R_m based on the two laser spot sizes is a function of g/κ_s. So the ratio of two R_m is used to obtain g/κ_s, and the R_m value for either of the two spot sizes can be used to extract the values of κ_s and g. This calculation process provides $\kappa_s = 37 \pm 12$ W/(m·K) and $g = 2.95 \pm 0.45$ MW/(m^2·K) for 1L WSe_2, based on the measurements using 100× and 40× lenses with spot sizes of 0.18 and 0.26 μm, respectively. Using this calculation method, the thermal conductivities and interfacial thermal conductance to the substrate for 2L−3L WSe_2 and the suspended 1L WSe_2 are obtained and summarized in Table 2 and Figure 4a,b.

The κ_s values of several layers of WSe_2 in our experimental studies are within the distribution range being approximately 20−37 W/(m·K), which is within the range of the published simulation results acquired by combining the first-principles calculations with the Boltzmann transport equation.[63] The thermal conductivity of WSe_2 is smaller than the other two common TMDC materials, MoS_2 and $MoSe_2$.[30] This is due to the increased atomic mass in WSe_2.[63] The thermal conductivity of WSe_2 also decreases with the layer number (Figure 4a) and the supported WSe_2 has a lower thermal conductivity than the suspended WSe_2. This decreasing trend of thermal conductivity was also discovered in the exfoliated hBN, MoS_2, and $MoSe_2$[23,30,34] (Figure 4c) and is attributed to the intrinsic scattering mechanism: Umklapp phonon scattering due to the crystal anharmonicity of phonons in thicker samples.[64] In addition, the phonon mean free path and the relative contribution from ballistic resistance decrease with the increase of layer.

Table 2. Thermal Conductivities and Interfacial Thermal Conductance of 1L−3L WSe_2

		thermal conductivity (W/(m·K))	interfacial thermal conductance (MW/(m^2·K))
1L WSe_2	suspended	37 ± 12	2.95 ± 0.46
1L WSe_2	suspended	49 ± 14	
2L WSe_2	supported	24 ± 12	3.45 ± 0.50
3L WSe_2	supported	20 ± 6	3.46 ± 0.45

Computational investigations were conducted in parallel to confirm the experimental investigations of the thermal conductivity of WSe_2 and its layer-dependent trend. Full-atom nonequilibrium molecular dynamics simulations (NEMD) were implemented on the atomistic model, as depicted in Figure 5a, where 1L and 2L WSe_2 with a length (in the x-direction) of 14.2 nm and a width (in the y-direction) of 8.2 nm in the AA stacking order are supported by an amorphous SiO_2 substrate. The heat flow was introduced in the x-direction to measure the thermal conductivity. Figure 5b demonstrates the thermal conductivities of 1L and 2L WSe_2, which are obtained with the heat flux, the overall temperature gradient along the heat flow direction (the inset), and the number of layers. For WSe_2, a decrease in the thermal conductivity is observed as the layer number increases from 1 to 2, which is consistent with the measurements. To investigate the phonon mechanisms, the vibrational density of states (VDOS) of the supported WSe_2 was calculated and is presented in Figure 5c. Compared to the VDOS of 1L WSe_2, the VDOS of 2L WSe_2 possesses two suppressed peaks at 5.2 and 8.2 THz, which indicates more severe phonon scattering, weaker phonon resonance, and thus degraded thermal conductivity. Figure 5d confirms the robustness of the decrease in the thermal conductivity with four different stacking orders, namely, AA, AB′, AA′, and AB. The experimental measurement, which is based on naturally exfoliated 2D WSe_2, is AA′ stacking. The computational process is detailed in the Supporting Information.

The computational investigation has confirmed the thermal conductivities of 2D WSe_2 and the decreasing trend with the layer number, which proves more severe phonon scattering from 1L to 2L WSe_2 from the view of vibrational density of states. To further investigate the layer-dependent trend of the thermal conductivities of the broad family of 2D materials, we provided the existing published studies of 2D materials' layer-dependent thermal conductivities in Table 3. It has been discovered that in the 2D regime, the exfoliated 2D materials' thermal conductivities have a decreasing trend with the layer

https://dx.doi.org/10.1021/acsami.0c21045
ACS Appl. Mater. Interfaces XXXX, XXX, XXX−XXX

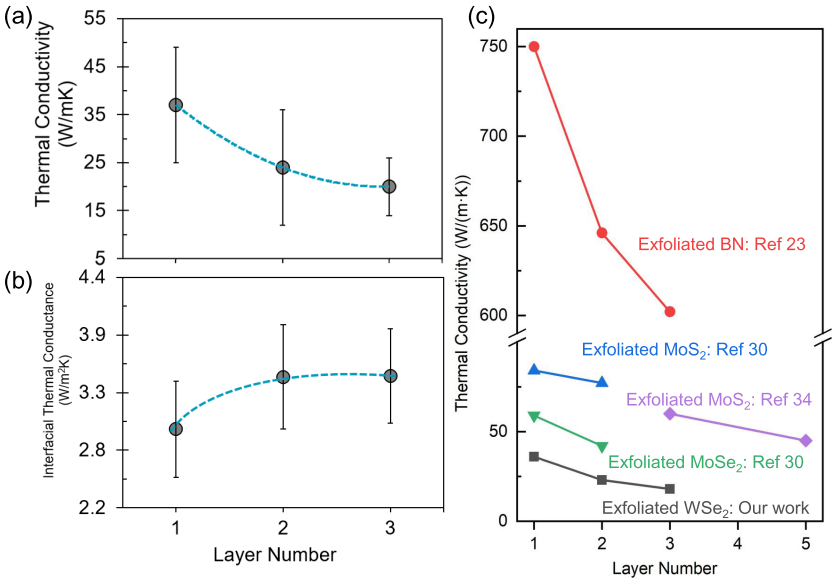

Figure 4. (a) Layer-dependent in-plane thermal conductivity and (b) interfacial thermal conductance of 1L−3L WSe_2. (c) Comparison of the layer-dependent thermal conductivity of common exfoliated 2D materials.[23,30,34]

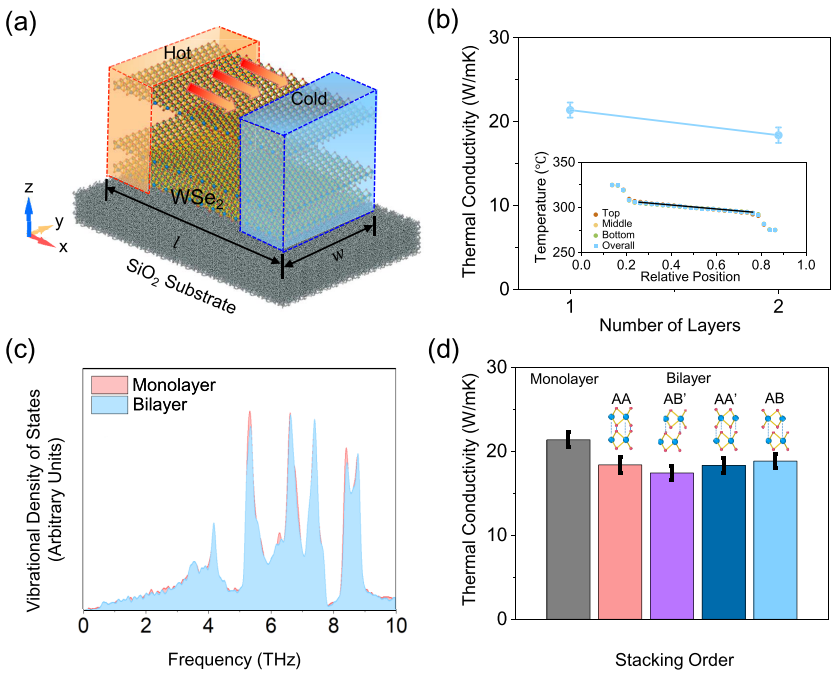

Figure 5. (a) Schematic of the atomistic modeling. (b) Thermal conductivity of WSe_2 as a function of the number of layers. (c) Vibrational density of states of 1L and 2L WSe_2. (d) Thermal conductivity of 2L WSe_2 with different stacking orders.

number,[23,30,34] whereas the chemical vapor deposition (CVD)-synthesized 2D materials' thermal conductivities have an increasing trend with the layer number.[66,67] Based on our computational investigation, this interesting opposite trend between exfoliated 2D materials and CVD 2D materials is due to the fact that exfoliated 2D materials are pristine. There are no grain boundaries in the exfoliated 2D materials, thus the Umklapp phonon scattering is dominant in the layer-dependent trend and the total thermal conductivity is limited by the Umklapp phonon scattering and edge boundary scattering. As a result, the 2D materials with a few layers possess thermal conductivities that are significantly higher than that of the bulk materials, which is around 1 W/(m·K),[55] whereas in the CVD 2D materials, there are grain boundaries that prevent the efficient thermal transport, thus the increasing layer number motivates more effective thermal transport paths.[68]

EXPERIMENTAL SECTION

The mechanical exfoliation method was used to produce 1L, 2L, and 3L WSe_2 from the bulk crystal (SPI supplies). The substrate is SiO_2 (285 nm)/Si. The suspended substrate is also the same substrate with a hole depth of 1 μm. The layer number of the WSe_2 sample was characterized by the tapping mode of atomic force microscopy (AFM) (Bruker Dimension), Raman spectroscopy, and photoluminescence.[33] A micro Raman spectrometer (RENISHAW inVia Raman Microscope system) was used for the thermal transport

https://dx.doi.org/10.1021/acsami.0c21045
ACS Appl. Mater. Interfaces XXXX, XXX, XXX−XXX

Table 3. Comparison of the Layer-Dependent Thermal Conductivity of Common 2D Materials (Exfoliated 2D Materials and CVD 2D Materials with Opposite Trends)

material	trend	thermal conductivity at RT (W/(m·K))	reference
exfoliated BN (1L−3L)	decreasing	1L: 750; 2L: 646; 3L: 602	23
exfoliated MoS_2 (1L and 2L)	decreasing	1L: 84; 2L: 77	30
exfoliated MoS_2 (3L−5L)	decreasing	3L: 60; 5L: 45	34
exfoliated $MoSe_2$ (1L and 2L)	decreasing	1L: 59; 2L: 42	30
computational studies of MoS_2 (1L−3L)	decreasing	1L: 155; 2L: 125; 3L: 115	65
CVD MoS_2 (1L and 2L)	increasing	1L: 13.3; 2L: 43.4	66
CVD WS_2 (1L and 2L)	increasing	1L: 32; 2L: 53	67

measurements. WSe_2 on the SiO_2/Si substrate was heated uniformly from 300 to 500 K by a temperature-controlled heating platform (Linkam Stage THMS600).

CONCLUSIONS

This work is the first experimental work about the in-plane thermal conductivities and interfacial thermal conductance of 1L−3L WSe_2, whereas all of the previous thermal studies of 2D WSe_2 are computational.[52−57] Our experimental method implemented an independent characterization of material absorbance and spot size and studied interfacial thermal conductance, a critical parameter that determines the energy dissipation in electronic devices, which ensures the precision of the measured value. These experimental results, along with the layer-dependent trend of thermal conductivities, are confirmed by our computational investigation using full-atom non-equilibrium molecular dynamics simulations. Our investigation of the thermal properties of 1L−3L WSe_2 has also addressed several important problems in the general thermal study of 2D materials with atomic thicknesses. First, the decreasing trend of the layer-dependent in-plane thermal conductivity and interfacial thermal conductance of exfoliated WSe_2 is investigated both experimentally and computationally and a trend approaching a constant is observed on the sample of three layers. This trend has been compared to CVD materials with analysis. Second, it confirms the theoretical prediction that WSe_2 has a relatively low in-plane thermal conductivity among the family of 2D materials, which proves that they are potential candidates for thermoelectrics. In general, we used the refined opto-thermal Raman technique to perform the first experimental study of the thermal transport properties of 1L−3L WSe_2 with computational confirmation. Specifically careful characterizations of the optical absorption coefficient, laser spot size, and thermal coupling to the substrate are conducted, which ensures a more robust thermal transport measurement in 2D materials. This work shed light on device modeling, thermal management, and quantum devices with enhanced performance.

ASSOCIATED CONTENT

Supporting Information

The Supporting Information is available free of charge at https://pubs.acs.org/doi/10.1021/acsami.0c21045.

Atomic force microscopy measurement of 1L−3L WSe_2; convection from the suspended material to air; computational modeling; and methodology (PDF)

AUTHOR INFORMATION

Corresponding Authors

Baoxing Xu − *Department of Mechanical and Aerospace Engineering, University of Virginia, Charlottesville, Virginia 22904, United States;* orcid.org/0000-0002-2591-8737; Email: bx4c@virginia.edu

Xian Zhang − *Department of Mechanical Engineering, Stevens Institute of Technology, Hoboken, New Jersey 07030, United States;* orcid.org/0000-0002-1088-4888; Email: xzhang4@stevens.edu

Authors

Elham Easy − *Department of Mechanical Engineering, Stevens Institute of Technology, Hoboken, New Jersey 07030, United States*

Yuan Gao − *Department of Mechanical and Aerospace Engineering, University of Virginia, Charlottesville, Virginia 22904, United States;* orcid.org/0000-0001-6030-9497

Yingtao Wang − *Department of Mechanical Engineering, Stevens Institute of Technology, Hoboken, New Jersey 07030, United States*

Dingkai Yan − *Department of Chemical Engineering and Materials Science, Stevens Institute of Technology, Hoboken, New Jersey 07030, United States*

Seyed M. Goushehgir − *Department of Mechanical Engineering, Urmia University of Technology, Urmia, West Azerbaijan, Iran*

Eui-Hyeok Yang − *Department of Mechanical Engineering, Stevens Institute of Technology, Hoboken, New Jersey 07030, United States;* orcid.org/0000-0003-4893-1691

Complete contact information is available at: https://pubs.acs.org/10.1021/acsami.0c21045

Author Contributions

The manuscript was written through contributions of all authors. All authors have given approval to the final version of the manuscript.

Notes

The authors declare no competing financial interest.

ACKNOWLEDGMENTS

This work was supported by Stevens Institute of Technology's startup funding, Stevens Institute of Technology's Bridging Award, Brookhaven National Laboratory Center for Functional Nanomaterials, Columbia Nano Initiative, and Office of Naval Research Young Investigator Program (grant number N00014-20-1-2611).

REFERENCES

(1) Novoselov, K. S.; Geim, A. K.; Morozov, S. V.; Jiang, D.; Zhang, Y.; Dubonos, S. V.; Grigorieva, I. V.; Firsov, A. A. Electric Field Effect in Atomically Thin Carbon Films. *Science* **2004**, *306*, 666−669.

(2) Novoselov, K. S.; Geim, A. K.; Morozov, S. V.; Jiang, D.; Katsnelson, M. I.; Grigorieva, I. V.; Dubonos, S. V.; Firsov, A. A. Two-Dimensional Gas of Massless Dirac Fermions in Graphene. *Nature* **2005**, *438*, 197−200.

(3) Novoselov, K. S.; Jiang, D.; Schedin, F.; Booth, T. J.; Khotkevich, V. V.; Morozov, S. V.; Geimm, A. K. Two-Dimensional Atomic Crystals. *Proc. Natl. Acad. Sci. U.S.A.* **2005**, *102*, 10451−10453.

(4) Geim, A. K.; Grigorieva, I. V. Van der Waals Heterostructures. *Nature* **2013**, *499*, 419−425.

(5) Wang, L.; Meric, I.; Huang, P. Y.; Gao, Q.; Gao, Y.; Tran, H.; Taniguchi, T.; Watanabe, K.; Campos, L. M.; Muller, D. A.; Guo, J.;

Kim, P.; Hone, J.; Shepard, K. L.; Dean, C. R. One-Dimensional Electrical Contact to a Two-Dimensional Material. *Science* **2013**, *342*, 614−617.
(6) Dean, C. R.; Young, A. F.; Meric, I.; Lee, C.; Wang, L.; Sorgenfrei, S.; Watanabe, K.; Taniguchi, T.; Kim, P.; Shepard, K. L.; Hone, J. Boron Nitride Substrate for High-Quality Graphene Electronics. *Nat. Nanotechnol.* **2010**, *5*, 722−726.
(7) Mayorov, A. S.; Gorbachev, R. V.; Morozov, S. V.; Britnell, L.; Jalil, R.; Ponomarenko, L. A.; Blake, P.; Novoselov, K. S.; Watanabe, K.; Taniguchi, T.; Geim, A. K. Micrometer-Scale Ballistic Transport in Encapsulated Graphene at Room Temperature. *Nano Lett.* **2011**, *11*, 2396−2399.
(8) Radisavljevic, B.; Radenovic, A.; Brivio, J.; Giacometti, V.; Kis, A. *Single-Layer MoS_2 Transistors*. *Nat. Nanotechnol.* **2011**, *6*, 147−150.
(9) Coleman, J. N.; Lotya, M.; O'Neill, A.; Bergin, S. D.; King, P. J.; Khan, U.; Young, K.; Gaucher, A.; De, S.; Smith, R. J.; Shvets, I. V.; Arora, S. K.; Stanton, G.; Kim, H. Y.; Lee, K.; Kim, G. T.; Duesberg, G. S.; Hallam, T.; Boland, J. J.; Wang, J. J.; Donegan, J. F.; Grunlan, J. C.; Moriarty, G.; Shmeliov, A.; Nicholls, R. J.; Perkins, J. M.; Grieveson, E. M.; Theuwissen, K.; McComb, D. W.; Nellist, P. D.; Nicolosi, V. Two-Dimensional Nanosheets Produced by Liquid Exfoliation of Layered Materials. *Science* **2011**, *331*, 568−571.
(10) Wang, Q. H.; Kalantar-Zadeh, K.; Kis, A.; Coleman, J. N.; Strano, M. S. Electronics and Optoelectronics of Two-Dimensional Transition Metal Dichalcogenides. *Nat. Nanotechnol.* **2012**, *7*, 699−712.
(11) Fang, H.; Chuang, S.; Chang, T. C.; Takei, K.; Takahashi, T.; Javey, A. High-Performance Single Layered WSe_2 p-FETs with Chemically Doped Contacts. *Nano Lett.* **2012**, *12*, 3788−3792.
(12) Britnell, L.; Ribeiro, R. M.; Eckmann, A.; Jalil, R.; Belle, B. D.; Mishchenko, A.; Kim, Y. J.; Gorbachev, R. V.; Georgiou, T.; Morozov, S. V.; Grigorenko, A. N.; Geim, A. K.; Casiraghi, C.; Neto, A. H. C.; Novoselov, K. S. Strong Light-Matter Interactions in Heterostructures of Atomically Thin Films. *Science* **2013**, *340*, 1311−1314.
(13) De VellisVellis, A.; Gritsenko, D.; Lin, Y.; Wu, Z. P.; Zhang, X.; Pan, Y. Y.; Xue, W.; Xu, J. Drastic sensing enhancement using acoustic bubbles for surface-based microfluidic sensors. *Sens. Actuators, B* **2017**, *243*, 298−302.
(14) Sun, D. Z.; Nguyen, A. E.; Barroso, D.; Zhang, X.; Preciado, E.; Bobek, S.; Klee, V.; Mann, J.; Bartels, L. Chemical vapor deposition growth of a periodic array of single-layer MoS_2 islands via lithographic patterning of an SiO_2/Si substrate. *2D Mater.* **2015**, *2*, No. 045014.
(15) Lee, G. H.; Cui, X.; Kim, Y. D.; Arefe, G.; Zhang, X.; Lee, C. H.; Ye, F.; Watanabe, K.; Taniguchi, T.; Kim, P.; Hone, J. Highly stable, dual-gated MoS_2 transistors encapsulated by hexagonal boron nitride with gate-controllable contact, resistance, and threshold voltage. *ACS Nano.* **2015**, *9*, 7019−7026.
(16) Wu, S. F.; Wang, L.; Lai, Y.; Shan, W. Y.; Aivazian, G.; Zhang, X.; Taniguchi, T.; Watanabe, K.; Xiao, D.; Dean, C.; Hone, J.; Li, Z. Q.; Xu, X. D. Multiple hot-carrier collection in photo-excited graphene Moiré superlattices. *Sci. Adv.* **2016**, *2*, No. e1600002.
(17) Wu, W. Z.; Wang, L.; Li, Y. L.; Zhang, F.; Lin, L.; Niu, S. M.; Chenet, D.; Zhang, X.; Hao, Y. F.; Heinz, T. F.; Hone, J.; Wang, Z. L. Piezoelectricity of single-atomic-layer MoS_2 for energy conversion and piezotronics. *Nature* **2014**, *514*, 470−474.
(18) Cui, X.; Lee, G. H.; Kim, Y. D.; Arefe, G.; Huang, P. Y.; Lee, C. H.; Chenet, D. A.; Zhang, X.; Wang, L.; Ye, F.; Pizzocchero, F.; Jessen, B. S.; Watanabe, K.; Taniguchi, T.; Muller, D. A.; Low, T.; Kim, P.; Hone, J. Multi-terminal transport measurements of MoS_2 using a van der Waals heterostructure device platform. *Nat. Nanotechnol.* **2015**, *10*, 534−540.
(19) Zhang, X.; Chenet, D.; Kim, B.; Yu, J.; Tang, J. Z.; Nuckolls, C.; Hone, J. Fabrication of hundreds of field effect transistors on a single carbon nanotube for basic studies and molecular devices. *J. Vac. Sci. Technol., B: Nanotechnol. Microelectron.: Mater., Process., Meas., Phenom.* **2013**, *31*, No. 06FI01.
(20) Balandin, A. A.; Ghosh, S.; Bao, W. Z.; Calizo, I.; Teweldebrhan, D.; Miao, F.; Lau, C. N. Superior Thermal Conductivity of Single-Layer Graphene. *Nano Lett.* **2008**, *8*, 902−907.
(21) Yuan, C.; Li, J. H.; Lindsay, L.; Cherns, D.; Pomeroy, J. W.; Liu, S.; Edgar, J. H.; Kuball, M. Modulating the thermal conductivity in hexagonal boron nitride via controlled boron isotope concentration. *Commun. Phys.* **2019**, *2*, No. 43.
(22) Gong, Y.; Zhang, Y.; Dudley, M.; Zhang, Y.; Edgar, J. H.; Heard, P. J.; Kuball, M. Thermal conductivity and Seebeck coefficients of icoshedral boron arsenide films on silicon carbide. *J. Appl. Phys.* **2010**, *108*, No. 084906.
(23) Cai, Q. R.; Scullion, D.; Gan, W.; Falin, A.; Zhang, S. Y.; Watanabe, K.; Taniguchi, T.; Chen, Y.; Santos, E. J. G.; Li, L. H. High thermal conductivity of high-quality monolayer boron nitride and its thermal expansion. *Sci. Adv.* **2019**, *5*, No. eaav0129.
(24) Eda, G.; Yamaguchi, H.; Voiry, D.; Fujita, T.; Chen, M. W.; Chhowalla, M. Photoluminescence from Chemically Exfoliated MoS_2. *Nano Lett.* **2011**, *11*, 5111−5116.
(25) Mak, K. F.; Lee, C.; Hone, J.; Shan, J.; Heinz, T. F. Atomically Thin MoS_2: A New Direct-Gap Semiconductor. *Phys. Rev. Lett.* **2010**, *105*, No. 136805.
(26) Splendiani, A.; Sun, L.; Zhang, Y. B.; Li, T. S.; Kim, J.; Chim, C. Y.; Galli, G.; Wang, F. Emerging Photoluminescence in Monolayer MoS_2. *Nano Lett.* **2010**, *10*, 1271−1275.
(27) Zhang, Y. J.; Ye, J. T.; Matsuhashi, Y.; Iwasa, Y. Ambipolar MoS_2 Thin Flake Transistors. *Nano Lett.* **2012**, *12*, 1136−1140.
(28) Tongay, S.; Zhou, J.; Ataca, C.; Lo, K.; Matthews, T. S.; Li, J. B.; Grossman, J. C.; Wu, J. Q. Thermally Driven Crossover from Indirect toward Direct Bandgap in 2D Semiconductors: $MoSe_2$ versus MoS_2. *Nano Lett.* **2012**, *12*, 5576−5580.
(29) Li, Y. L.; Chernikov, A.; Zhang, X.; Rigosi, A.; Hill, H. M.; Zande, A. M. V. D.; Chenet, D. A.; Shih, E. M.; Hone, J.; Heinz, T. F. Measurement of the optical dielectric function of monolayer transition-metal dichalcogenides: MoS_2, $MoSe_2$, WS_2, WSe_2. *Phys. Rev. B* **2014**, *90*, No. 205422.
(30) Zhang, X.; Sun, D. Z.; Li, Y. L.; Lee, G. H.; Cui, X.; Chenet, D.; You, Y. M.; Heinz, T. F.; Hone, J. C. Measurement of lateral and interfacial thermal conductivity of single- and bilayer MoS_2 and $MoSe_2$ using optothermal Raman technique. *ACS Appl. Mater. Interfaces* **2015**, *7*, 25923−25929.
(31) Yin, D. Q.; Dun, C. C.; Gao, X.; Liu, Y.; Zhang, X.; Carroll, D. L.; Swihart, M. T. Controllable colloidal synthesis of Tin(II) chalcogenide nanocrystals and their solution-processed flexible thermoelectric thin films. *Small.* **2018**, *14*, No. 1801949.
(32) Li, Y.; Ye, F.; Xu, J.; Zhang, W.; Feng, P. X. L.; Zhang, X. Gate-tuned temperature in a hexagonal boron nitride-encapsulated 2D semiconductor devices. *IEEE Trans. Electron Devices* **2018**, *65*, 4068−4072.
(33) Zhang, X. Characterization of layer number of two-dimensional transition metal diselenide semiconducting devices using Si-peak analysis. *Adv. Mater. Sci. Eng.* **2019**, *2019*, No. 7865698.
(34) Yuan, P. Y.; Wang, R. D.; Wang, T. Y.; Wang, X. W.; Xie, Y. S. Nonmonotonic thickness-dependence of in-plane thermal conductivity of few-layered MoS_2: 2.4 to 37.8 nm. *Phys. Chem. Chem. Phys.* **2018**, *20*, 25752−25761.
(35) Jo, I.; Pettes, M. T.; Ou, E.; Wu, W.; Shi, L. Basel-plane thermal conductivity of few-layer molybdenum disulfide. *Appl. Phys. Lett.* **2014**, *104*, No. 201902.
(36) Bae, J. J.; Jeong, H. Y.; Han, G. H.; Kim, J.; Kim, H.; Kim, M. S.; Moon, B. H.; Lim, S. C.; Lee, Y. H. Thickness-dependent in-plane thermal conductivity of suspended MoS_2 grown by chemical vapor deposition. *Nanoscale* **2017**, *9*, 2541−2547.
(37) Cai, W. W.; Moore, A. L.; Zhu, Y. W.; Li, X. S.; Chen, S. S.; Shi, L.; Ruoff, R. S. Thermal Transport in Suspended and Supported Monolayer Graphene Grown by Chemical Vapor Deposition. *Nano Lett.* **2010**, *10*, 1645−1651.
(38) Gu, X. K.; Yang, R. G. Phonon transport in single-layer transition metal dichalcogenides: A first-principles study. *Appl. Phys. Lett.* **2014**, *105*, No. 131903.
(39) Liu, J.; Choi, G. M.; Cahill, D. G. J. Measurement of the anisotropic thermal conductivity of molybdenum disulfide by the

https://dx.doi.org/10.1021/acsami.0c21045
ACS Appl. Mater. Interfaces XXXX, XXX, XXX−XXX

time-resolved magneto-optic Kerr effect. *Appl. Phys.* **2014**, *116*, No. 233107.
(40) Zhang, J. C.; Hong, Y.; Wang, X. Y.; Yue, Y. N.; Xie, D. M.; Jiang, J.; Xiong, Y. H.; Li, P. S. Phonon Thermal Properties of Transition-Metal Dichalcogenides MoS_2 and $MoSe_2$ Heterostructure. *J. Phys. Chem. C* **2017**, *121*, 10336−10344.
(41) Yan, R. S.; Simpson, J. R.; Bertolazzi, S.; Brivio, J.; Watson, M.; Wu, X. F.; Kis, A.; Luo, T. F.; Walker, A. R. H.; Xing, H. G. Thermal conductivity of monolayer molybdenum disulfide obtained from temperature-dependent Raman spectroscopy. *ACS Nano* **2014**, *8*, 986−993.
(42) Zobeiri, H.; Wang, R. D.; Wang, T. Y.; Lin, H.; Deng, C.; Wang, X. W. Frequency-domain energy transport state-resolved Raman for measuring the thermal conductivity of suspended nm-thick $MoSe_2$. *Int. J. Heat Mass Transf.* **2019**, *133*, 1074−1085.
(43) Peng, B.; Zhang, H.; Shao, H. Z.; Xu, Y. C.; Zhang, X. C.; Zhu, H. Y. Thermal conductivity of monolayer MoS_2, $MoSe_2$, and WS_2: interplay of mass effect, interatomic bonding and anharmonicity. *RSC Adv.* **2016**, *6*, 5767−5773.
(44) Zhou, H. L.; Wang, C.; Shaw, J. C.; Cheng, R.; Chen, Y.; Huang, X. Q.; Liu, Y.; Weiss, N. O.; Lin, Z. Y.; Huang, Y.; Duan, X. F. Large area growth and electrical properties of p-type WSe_2 atomic layers. *Nano Lett.* **2015**, *15*, 709−713.
(45) Seyler, K. L.; Schaibley, J. R.; Gong, P.; Rivera, P.; Jones, A. M.; Wu, S. F.; Yan, J. Q.; Mandrus, D. G.; Yao, W.; Xu, X. D. Electrical control of second-harmonic generation in a WSe_2 monolayer transistor. *Nat. Nanotechnol.* **2015**, *10*, 407−411.
(46) Yuan, H. T.; Wang, X. Q.; Lian, B.; Zhang, H. J.; Fang, X. F.; Shen, B.; Xu, G.; Xu, Y.; Zhang, S. C.; Hwang, H. Y.; Cui, Y. Generation and electric control of spin−valley-coupled circular photogalvanic current in WSe_2. *Nat. Nanotechnol.* **2014**, *9*, 851−857.
(47) Si, M. W.; Jiang, C. S.; Chung, W.; Du, Y. C.; Alam, M. A.; Ye, P. D. Steep-Slope WSe_2 Negative Capacitance Field-Effect Transistor. *Nano Lett.* **2018**, *18*, 3682−3687.
(48) Cho, I. T.; Kim, J. I.; Hong, Y.; Roh, J.; Shin, H.; Baek, G. W.; Lee, C.; Hong, B. H.; Jin, S. H.; Lee, J. H. Low frequency noise characteristics in multilayer WSe_2 field effect transistor. *Appl. Phys. Lett.* **2015**, *106*, No. 023504.
(49) Yamamoto, M.; Nouchi, R.; Kanki, T.; Hattori, A. N.; Watanabe, K.; Taniguchi, T.; Ueno, K.; Tanaka, H. Gate-Tunable Thermal Metal−Insulator Transition in VO_2 Monolithically Integrated into a WSe_2 Field-Effect Transistor. *ACS Appl. Mater. Interfaces* **2019**, *11*, 3224−3230.
(50) Kang, W.-M.; Lee, S. T.; Cho, I. T.; Park, T. H.; Shin, H.; Hwang, C. S.; Lee, C.; Park, B. G.; Lee, J. H. Multi-layer WSe_2 field effect transistor with improved carrier-injection contact by using oxygen plasma treatment. *Solid State Electron* **2018**, *140*, 2−7.
(51) Huang, J. N.; Hoang, T. B.; Mikkelsen, M. H. Probing the origin of excitonic states in monolayer WSe_2. *Sci. Rep.* **2016**, *6*, No. 22414.
(52) Wang, J.; Xie, F.; Cao, X. H.; An, S. C.; Zhou, W. X.; Tang, L. M.; Chen, K. Q. Excellent Thermoelectric Properties in monolayer WSe_2 Nanoribbons due to Ultralow Phonon Thermal Conductivity. *Sci. Rep.* **2017**, *7*, No. 41418.
(53) Yuan, K. P.; Zhang, X. L.; Li, L.; Tang, D. W. Effects of tensile strain and finite size on thermal conductivity in monolayer WSe_2. *Phys. Chem. Chem. Phys.* **2019**, *21*, 468−477.
(54) Chan, H.; Sasikumar, K.; Srinivasan, S.; Cherukara, M.; Narayanan, B.; Sankaranarayanan, S. K. R. S. Machine learning a bond order potential model to study thermal transport in WSe_2 nanostructures. *Nanoscale* **2019**, *11*, 10381−10392.
(55) Kumar, S.; Schwingenschlögl, U. Thermoelectric Response of Bulk and Monolayer $MoSe_2$ and WSe_2. *Chem. Mater.* **2015**, *27*, 1278−1284.
(56) Zhou, W. X.; Chen, K. Q. First-Principles Determination of Ultralow Thermal Conductivity of monolayer WSe_2. *Sci. Rep.* **2015**, *5*, No. 15070.
(57) Norouzzadeh, P.; Singh, D. J. Thermal conductivity of single-layer WSe_2 by a Stillinger−Weber potential. *Nanotechnology* **2017**, *28*, No. 075708.
(58) Mavrokefalos, A.; Nguyen, N. T.; Pettes, M. T.; Johnson, D. C.; Shi, L. In-plane thermal conductivity of disordered layered WSe_2 and (W)x(WSe_2)y superlattice films. *Appl. Phys. Lett.* **2007**, *91*, No. 171912.
(59) Chiritescu, C.; Cahill, D. G.; Nguyen, N.; Johnson, D.; Bodapati, A.; Keblinski, P.; Zschack, P. Ultralow thermal conductivity in disordered, layered WSe_2 crystals. *Science* **2007**, *315*, 351−353.
(60) Jiang, P. Q.; Qian, X.; Gu, X. K.; Yang, R. G. Probing Anisotropic Thermal Conductivity of Transition Metal Dichalcogenides MX2 (M = Mo, W and X = S, Se) using Time-Domain Thermoreflectance. *Adv. Mater.* **2017**, *29*, No. 1701068.
(61) Olson, D.; Braun, J. L.; Hopkins, P. Probing Anisotropic Thermal Conductivity of Transition Metal Dichalcogenides MX_2 (M = Mo, W and X = S, Se) using Time-Domain Thermoreflectance. *J. Appl. Phys.* **2019**, *126*, No. 150901.
(62) Jin-Xiang, D.; Xiao-Kang, Z.; Qian, Y.; Xu-Yang, W.; Guang-Hua, C.; De-Yan, H. Optical properties of hexagonal boron nitride thin films deposited by radio frequency bias magnetron sputtering. *Chin. Phys. B* **2009**, *18*, 4013−4018.
(63) Zulfiqar, M.; Zhao, Y. C.; Li, G.; Li, Z. C.; Ni, J. Intrinsic Thermal conductivities of monolayer transition metal dichalcogenides MX_2 (M = Mo, W; X = S, Se, Te). *Sci. Rep.* **2019**, *9*, No. 4571.
(64) Cao, H. Y.; Guo, Z. X.; Xiang, H. J.; Gong, X. G. Layer and size dependence of thermal conductivity in multilayer graphene nanoribbons. *Phys. Lett. A* **2012**, *376*, 525−528.
(65) Gu, X. K.; Li, B. W.; Yang, R. G. J. Layer thickness-dependent phonon properties and thermal conductivity of MoS_2. *Appl. Phys.* **2016**, *119*, No. 085106.
(66) Bae, J. J.; Jeong, H. Y.; Han, G. H.; Kim, J.; Kim, H.; Kim, M. S.; Moon, B. H.; Lim, S. C.; Lee, Y. H. Thickness-dependent in-plane thermal conductivity of suspended MoS_2 grown by chemical vapor deposition. *Nanoscale* **2017**, *9*, 2541−2547.
(67) Peimyoo, N.; Shang, J. Z.; Yang, W. H.; Wang, Y. L.; Cong, C. X.; Yu, T. Thermal conductivity determination of suspended mono- and bilayer WS_2 by Raman spectroscopy. *Nano Res.* **2015**, *8*, 1210−1221.
(68) Zhou, S. W.; Tao, X.; Gu, Y. Thickness-Dependent Thermal Conductivity of Suspended Two Dimensional Single-Crystal In_2Se_3 Layers Grown by Chemical Vapor Deposition. *J. Phys. Chem. C* **2016**, *120*, 4753−4758.
(69) Kumar, S.; Schwingenschlogl, U. Thermoelectric Response of Bulk and Monolayer $MoSe_2$ and WSe_2. *Chem. Mater.* **2015**, *27*, 1278−1284.
(70) Roy, S.; Sharbirin, A.; Lee, Y.; Kim, W. B.; Kim, T. S.; Cho, K.; Kang, K.; Jung, H. S.; Kim, J. Measurement of Quantum Yields of Monolayer TMDs Using Dye-Dispersed PMMA Thin Films. *Nanomaterials* **2020**, *10*, 1032.
(71) Mohamed, N. B.; Wang, F.; Lim, H. E.; Zhang, W.; Koirala, S.; Mouri, S.; Miyauchi, Y.; Matsuda, K. Evaluation of Photoluminescence Quantum Yield of Monolayer WSe_2 Using Reference Dye of 3-Borylbithiophene derivative. *Phys. Status Solidi B* **2017**, *254*, No. 1600563.
(72) Amani, M.; Taheri, P.; Addou, R.; Ahn, G. H.; Kiriya, D.; Lien, D.-H.; Ager, J. W., III; Wallace, R. M.; Javey, A. Recombination Kinetics and Effects of Superacid Treatment in Sulfurand Selenium-Based Transition Metal Dichalcogenides. *Nano Lett.* **2016**, *16*, 2786−2791.
(73) Kim, H.; Ahn, G. H.; Cho, J.; Amani, M.; Mastandrea, J. P.; Groschner, C. K.; Lien, D. H.; Zhao, Y. B.; Ager, J. W.; Scott, M. C.; et al. Synthetic WSe_2 Monolayers with High Photoluminescence Quantum Yield. *Sci. Adv.* **2019**, *5*, No. eaau4728.

https://dx.doi.org/10.1021/acsami.0c21045
ACS Appl. Mater. Interfaces XXXX, XXX, XXX−XXX